PERGAMON

International Journal of Heat and Mass Transfer 46 (2003) 809–821

International Journal of HEAT and MASS TRANSFER

www.elsevier.com/locate/ijhmt

Three-dimensional computational analysis of gas and heat transport phenomena in ducts relevant for anode-supported solid oxide fuel cells

Jinliang Yuan, Masoud Rokni, Bengt Sundén *

Division of Heat Transfer, Lund Institute of Technology, Box 118, S-221 00 Lund, Sweden

Received 1 July 2002; received in revised form 20 August 2002

Abstract

Various transport phenomena occurring in an anode duct of medium temperature solid oxide fuel cell (SOFC) have been simulated and analyzed by a fully three-dimensional calculation method. The considered composite duct consists of a thick porous layer, the gas flow duct and solid current interconnector. Unique fuel cell boundary and interfacial conditions, such as the combined thermal boundary conditions on solid walls, mass transfer associated with the electrochemical reaction and gas permeation across the interface, were applied in the analysis. Based on three characteristic ratios proposed in this study, gas flow and heat transfer were investigated and presented in terms of friction factors and Nusselt numbers. It was revealed that, among various parameters, the duct configuration and properties of the porous anode layer have significant effects on both gas flow and heat transfer of anode-supported SOFC ducts. The results from this study can be applied in fuel cell overall modeling methods, such as those considering unit/stack level modeling.

1. Introduction

Uniform supply of species to an active surface, where the electrochemical reaction happens, is important in a fuel cell duct. The most common ducts in fuel cells consist of a porous layer, the flow duct and solid current collector (or connector) with constant cross-section area. Understanding of various gas and heat transport processes is crucial for increasing power density, reducing manufacturing cost and accelerating commercialisation of fuel cell systems. Among various fuel cells, high temperature fuel cells (e.g., solid oxide fuel cells (SOFCs)) have very different features, such as reduction of activation polarisation, elimination of expensive catalysts and potential integration with bottoming cycle/cogeneration system. Many technical challenges associated with low temperature fuel cells (e.g., proton exchange membrane fuel cells) can be eliminated, but different limitations arise, such as the need of a long start-up transient time and high manufacturing cost.

A new trend during recent years is to lower the SOFC operating temperature to a moderate range (700–850 °C) by employing a thick porous anode (1.5–2 mm) as the supporting structure [1–4]. It has been revealed that the principal loss in this design is attributed to the concentration polarization related to gaseous species transport through the porous anode [1], because the size of the porous anode is bigger than that of the flow duct in terms of the thickness and cross-section area. In the porous anode layer, the transport rate of fuel gases is controlled by various parameters, such as its microstructure (e.g., pore size, permeability, volume percent porosity), pressure gradient between the flow duct and porous layer, gas composition and inlet conditions etc. As will be clarified later in this paper, the duct geometry characteristics will have significant effects as well.

Fundamental studies of forced convective heat transfer and gas flow, where the porous media appear, have been considered by various investigators in recent

* Corresponding author.

0017-9310/03/$ - see front matter
PII: S0017-9310(02)00357-5

Nomenclature

a	width of porous layer, m
b	width of flow duct, m
B	microscopic inertial coefficient, 1/m
D_h	hydraulic diameter, m
D_{hr}	diameter ratio
f	Fanning friction factor
F	the Forchheimer coefficient
h_d	height of the duct, m
h_b	heat transfer coefficient, W/(m^{2}K)
h_p	thickness of porous layer, m
h_r	thickness ratio (h_p/h)
k	thermal conductivity, W/(mK)
k_r	thermal conductivity ratio (k_{eff}/k_f)
$\overline{Nu}_b$	spanwise average Nusselt number
P	pressure, Pa
PL_r	permeation length ratio
PR_r	permeation rate ratio
q_b	heat flux, W/(m^2)
Re	Reynolds number (UD_h/v)
S	source term
T	temperature, K
U_i	velocity components in x, y and z directions, respectively, m/s
V_m	mass transfer velocity at bottom wall, m/s
V_p	permeation velocity across interface, m/s
x, y, z	Cartesian coordinates
x^*	hydrodynamic dimensionless axial distance ($x/(D_hRe)$)
x^{**}	thermal dimensionless axial distance (x^*/Pr)

Greek symbols

β	permeability of diffusion layer, m^2
ε	porosity
μ	dynamic viscosity, kg/(m s)
v	kinematic viscosity, m^2/s
ρ	density, kg/m^3

Subscripts

a	anode
b	bottom wall
bulk	bulk fluid condition
c	cathode
eff	effective parameter
f	fluid
H_2O	water vapour
in	inlet
m	mass transfer
p	porous layer or permeation
s	solid current connector

years (see [5–8]). This is so because a better understanding of thermal engineering applications is required where porous materials are present. Because of the simplicity and reasonable performance within a certain range of applications, the Darcy model has been used for the majority of existing studies on gas flow and heat transfer in porous media. For a single-phase fully developed flow through a porous medium, the Darcy model has a linear feature, i.e., the volumetrically averaged velocity in any direction in space is proportional to the pressure gradient in that direction, and inversely proportional to the viscosity. It has been found that the Darcy model has some limitations, e.g., it does not satisfy the no-slip condition at a solid wall, and breaks down also due to the increasing role of inertial forces. It was found that the inertial forces should be taken into account when the interstitial flow velocity (i.e., the flow through pores of a porous medium) is not small, based on pore Reynolds number [6]. It was revealed in [7] that heat transfer can be significantly affected by the effective thermal conductivity and Darcy number of the porous medium. Various types of interfacial conditions between a porous medium and a gas flow duct were analyzed in detailed for both gas flow and heat transfer in [8]. It is clear that part of the gas flow penetrates into the porous layer and the remaining gas flows downstream at decreasing flow rates. The static pressure in such a duct then changes along the main flow due to the following reasons: the friction between the gas flow and the internal surfaces of the duct creates pressure drop, and the mass permeation across the interface between the flow duct and the porous layer implies that mass and momentum are transferred from/into the porous layer [9]. The latter one complicates the transport processes further even in a simple duct flow, because it is a mass changing process and depends on the pressure gradient between the flow duct and porous layer. This process is usually considered as an overall mass transport with a constant permeability.

In the fuel cell anode duct, another factor should be considered, because part of the fuel (e.g., H_2) is consumed and water (H_2O) is generated in the electrochemical reaction. This is usually simulated as a constant mass suction and injection V_m (or $Re_m = V_mD_h/v$), respectively, at the permeable wall in the anode side (see [10]). When mass suction occurs, decrease in pressure drop and increase in Nusselt number have been revealed in [10], while increase in pressure drop and decrease in Nusselt number holds for the case of mass injection from the duct.

During recent years, simulations and analyses of mass and heat transport have been presented for various

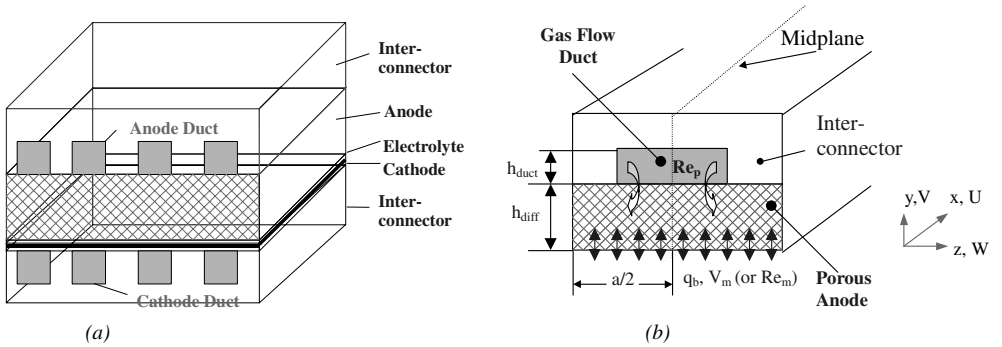

Fig. 1. (a) Structure of a unit cell, (b) schematic drawing of a composite anode duct under investigation.

SOFC flow ducts in the literature, in terms of gas utilization, produced power energy efficiency, electrical current, temperature distribution, but mainly for electrolyte-supported design with thin electrode layers (see [10,11] and references therein). A literature survey has been conducted to cover the relevant problems of heat transfer and mass transport modelling. It was found that there is no study simulating and analysing heat transfer and pressure drop in anode-supported fuel cell ducts where a thick porous anode appears. To extend the previous studies of the current authors, the present paper describes a fully three-dimensional numerical investigation of gas flow and heat transfer in the medium temperature SOFC anode duct including the porous layer and the solid interconnectors. One objective of this paper is to develop such an analysis method to understand the various transport processes in ducts for anode-supported SOFCs, with an emphasis on the friction factor f and Nusselt number Nu. The unique boundary conditions of the fuel cell such as thermal (heat generation) and mass (suction/injection) transport at the permeable walls, and the interface conditions are employed in the investigation. The Forchheimer-extended Darcy model has been applied in this study to assess the inertial force effects. Based on three characteristic ratios, studies have been conducted for various engineering parameters which are relevant for the anode-supported SOFC design, and effects on the gas flow and heat transfer are presented and discussed in terms of various parameters, such as the friction factor and Nusselt number, permeation Reynolds number.

2. Problem statement and formulation

2.1. Problem statement and assumptions

A three-dimensional computational fluid dynamics (CFD) code is employed to solve the Navier–Stokes equations, mass conservation equation and energy equation for an anode duct of a typical anode-supported SOFC design (see Fig. 1(a)). Fig. 1(b) shows the schematic structure of the anode duct. The duct consists of a thick porous anode layer, the gas flow duct and solid current interconnector. The U, V, and W are the velocity components in the x, y, z directions, respectively. For simplicity, a steady laminar flow of an incompressible fluid is considered and all thermal–physical properties are assumed constant. In this study, the porous anode layer is assumed to be homogeneous and characterized by effective parameters, such as porosity, permeability and thermal conductivity, and the fluid in the porous layer is in thermal equilibrium with the solid matrix. A chemical reaction appears at the porous surface in contact with the electrolyte (bottom surface in Fig. 1(b)). A constant flow rate $U = U_{\text{in}}$ is specified at the inlet of the gas flow duct, while $U = 0$ is specified at the inlet for the interconnector and porous anode layer. Only the right half of the duct is considered by imposing symmetry conditions on the mid-plane.

2.2. Governing equations

The governing equations of gas flow and heat transfer are the continuity, momentum and energy equations, which are written as

$$\partial(\rho_{\text{eff}} U_i)/\partial x_i = S_{\text{m}} \tag{1}$$

$$\frac{\partial\left(\rho_{\text{eff}} U_j U_i\right)}{\partial x_j} = -\frac{\partial P}{\partial x_i} + \frac{\partial}{\partial x_j}\left(\mu_{\text{eff}}\left(\frac{\partial U_i}{\partial x_j} + \frac{\partial U_j}{\partial x_i}\right)\right) + S_{\text{d}i} \tag{2}$$

$$\frac{\partial\left(\rho_{\text{eff}} U_j T\right)}{\partial x_j} = \frac{\partial}{\partial x_j}\left(\frac{k_{\text{eff}}}{c_{\text{p eff}}}\frac{\partial T}{\partial x_j}\right) \tag{3}$$

All the properties above with subscript eff mean effective values. A source term S_{m} in the mass conservation equation is included to account for the mass transfer caused by the electrochemical reaction from/to the porous anode layer (bottom surface). The detailed

procedure concerning this source term was discussed in [10,11], and the final form is as follows:

$$S_{\mathrm{m}} = \frac{\partial U_{\mathrm{bulk}}}{\partial x} = Re_{\mathrm{m}} \frac{v}{D_{\mathrm{h}}} \frac{a}{A} \tag{4}$$

where U_{bulk} is the bulk fluid velocity in the flow duct, Re_{m} wall Reynolds number ($Re_{\mathrm{m}} = V_{\mathrm{m}} D_{\mathrm{h}}/v$, positive value for the case of injection and negative for the suction), D_{h} hydraulic diameter. The other variables can be found in the nomenclature list. The momentum equation has been modified to be valid for both the porous layer and the flow duct, by including a source term $S_{\mathrm{d}i}$

$$S_{\mathrm{d}i} = -(\mu_{\mathrm{eff}} U_i/\beta) - \rho_{\mathrm{eff}} B U_i |\vec{U}| \tag{5}$$

In Eq. (5), β is the porous layer permeability, and U_i represents the volume-averaged velocity components. The first term on the right-hand side accounts for the linear relationship between the pressure gradient and flow rate by the Darcy law, while the second term is the Forchheimer term taking into account the inertial effects, i.e., the non-linear relationship between pressure drop and flow rate. The inertial coefficient B in the second term is an empirical function depending on the microstructure of the porous medium. A review can be found in [5]. It should be noted that Eqs. (1)–(3) are formulated to be generally valid for both the main duct and the porous layer. The source term in Eq. (2) is zero in the flow duct.

2.3. Additional equations

The Fanning friction factor f of the gas flow in the duct is defined as

$$f = -\frac{1}{2} \frac{D_{\mathrm{h}}}{\rho U_{\mathrm{bulk}}^2} \frac{\mathrm{d}P}{\mathrm{d}x} \tag{6}$$

where $\mathrm{d}P/\mathrm{d}x$ is the pressure gradient along the main flow direction. As mentioned above, the mass permeation across the interface between the flow duct and the porous anode layer contributes to the pressure change along the main flow direction. Based on the fact that the mass permeation is small (i.e., interface permeation Reynolds number $Re_{\mathrm{p}} = V_{\mathrm{p}} D_{\mathrm{h}}/v < Re_{\mathrm{in}}$), the deduced pressure change can be written as

$$\left(\frac{\mathrm{d}P}{\mathrm{d}x}\right)_{\mathrm{p}} = -\rho U_{\mathrm{bulk}} \left(\frac{\partial U_{\mathrm{bulk}}}{\partial x}\right) \mathrm{d}x \tag{7}$$

The Nusselt number Nu_{b} at the heated wall is

$$\overline{Nu}_{\mathrm{b}} = \frac{\bar{h}_{\mathrm{b}} D_{\mathrm{h}}}{k_{\mathrm{eff}}} = \frac{q_{\mathrm{b}} D_{\mathrm{h}}}{k_{\mathrm{eff}} (\overline{T}_{\mathrm{b}} - T_{\mathrm{bulk}})} \tag{8}$$

q_{b} is the heat flux at the bottom wall, and specified to a constant value in this work; T_{b} heated wall spanwise average temperature, T_{bulk} the mean stream-wise flow temperature in the cross-section,

$$T_{\mathrm{bulk}} = \frac{\int T|U| \,\mathrm{d}A}{\int |U| \,\mathrm{d}A} \tag{9}$$

2.4. Boundary and interfacial conditions

Based on the fuel cell function, the unique thermal and mass transfer boundary conditions at the walls have been clarified in [11] and are implemented in this study:

$$U = V - V_{\mathrm{m}} = W = 0, \quad -k_{\mathrm{eff}} \frac{\partial T}{\partial y} = q_{\mathrm{b}} \quad \text{at bottom wall } (y = 0) \tag{10}$$

$$U = V = W = 0, \quad q = 0 \text{ at top and side walls} \tag{11}$$

$$\frac{\partial U}{\partial z} = \frac{\partial V}{\partial z} = W = \frac{\partial T}{\partial z} = 0 \quad \text{at mid-plane } (z = a/2) \tag{12}$$

The interfacial conditions between the porous anode layer and flow duct have been extensively studied in the literature. For example, one of the early attempts revealed a slip in the velocity at the interface region, commonly called Beavers–Joseph condition [8]. A detailed literature survey for various interfacial conditions can also be found in [8]. In the present investigation, the interfacial boundary conditions, commonly employed in the literature and including the continuity of velocity, shear stress, temperature, and heat flux, are applied as follows:

$$U_- = U_+, \quad (\mu_{\mathrm{eff}} \partial U/\partial y)_- = (\mu_{\mathrm{f}} \partial U/\partial y)_+ \tag{13}$$

$$T_- = T_+, \quad (k_{\mathrm{eff}} \partial T/\partial y)_- = (k_{\mathrm{f}} \partial T/\partial y)_+ \tag{14}$$

Here subscript + (plus) stands for fluid side, − (minus) for porous layer side. Moreover, the thermal interfacial condition, Eq. (14), is also applied at an interface between the porous media and the solid current interconnector with k_{s} instead of k_{f}.

2.5. Characteristic ratios

Three characteristic ratios, having significant effects on various transport processes as discussed later in this paper, are defined in this section. These are the hydraulic diameter ratio D_{hr} (ratio of the porous layer diameter to the flow duct diameter), the permeation length ratio $\mathrm{PL_r}$ (ratio of the porous layer width to the flow duct width), and the permeation rate ratio $\mathrm{PR_r}$ (ratio of the entrance pressure gradient to permeation resistance).

$$D_{\mathrm{hr}} = D_{\mathrm{hp}}/D_{\mathrm{hd}} \tag{15}$$

$$\mathrm{PL_r} = a/b \tag{16}$$

$$PR_r = (\rho U_{in}^2/2h_p)/(\mu U_{in}/\beta) = (\rho\beta U_{in})/(2\mu h_p) \quad (17)$$

D_{hp} in Eq. (15) is the hydraulic diameter of the porous anode layer, D_{hd} the hydraulic diameter of the flow duct; a in Eq. (16) is the width of porous layer, b the width of the flow duct; h_p in Eq. (17) is the thickness of the porous layer. It is clear that both diameter ratio D_{hr} and permeation length ratio PL_r are related to the flow duct and porous anode layer configurations, to account for the characteristics of the permeation area and length, respectively. The permeation rate ratio PR_r considers the characteristics of the porous anode material (such as the permeability β) and duct operation parameter (such as the inlet velocity U_{in}).

3. Numerical solution procedure

A three-dimensional CFD code was used to solve the Eqs. (1)–(3), together with the boundary conditions (10)–(12) and interfacial conditions (13) and (14). The code was originally developed in [13] and further developed in [14]. It is a general purpose code based on the finite-volume technique with boundary fitted coordinates for solving the differential equations. The Cartesian coordinate system in the physical space is replaced by a general non-orthogonal coordinate system. The momentum equations are solved for the velocity components on a non-staggered grid arrangement. The Rhie–Chow interpolation method is used to compute the velocity components at the control volume faces. Algorithms based on the TDMA and a modified SIP are employed for solving the algebraic equations. In this work, the convective terms are treated by the QUICK scheme, while the diffusive terms are treated by the central difference scheme. The SIMPLEC algorithm handles the linkage between velocities and pressure. The source term in Eq. (1), accounting for mass transfer effects, is zero in most of the regions, and non-zero only in the regions neighboring boundaries, where mass transfer caused by the electrochemical reaction occurs (bottom wall in Fig. 1(b)). The continuity Eq. (1) also presents an additional constraint to deduce the pressure gradient of the momentum Eq. (2) in the main flow direction. Procedures to obtain a corrected averaged axial velocity by the deduced pressure gradient have been documented in [12] also, when mass transfer is considered. It is clear that no gas flow is present in the solid interconnector. Eqs. (1) and (2) are then blocked out and only the heat conduction equation, derived from the energy Eq. (3), is solved for this domain. In this investigation, a uniform grid point distribution in the cross-section is applied. To obtain finer meshes in the entrance region of the duct, a non-uniform distribution of grid points with an expansion factor is implemented for the main flow direction. Various values of the expansion factor have been checked and 1.01 was found to be sufficient for independent grid distribution.

Parameters of anode-supported SOFCs and the porous medium, appearing in the common literature, are applied as a base case in this study. Duct geometries, adopted in [2], are employed as follows: length of the duct $L = 20$ mm; width of the porous layer $a = 2$ mm, and its thickness $h_p = 2$ mm; while the width of the flow duct is $b = 1$ mm, and its height $h_d = 1$ mm. Fuel gas is 0.80 mole fraction of H_2, and 0.20 mole fraction of water vapour with inlet temperature $T_{in} = 700$ °C; For the porous layer, one has: thermal conductivity ratio $k_r(= k_{eff}/k_f) = 1$, effective dynamic viscosity $\mu_{eff} = \mu_f = 2.3 \times 10^{-5}$ kg/(ms), porosity $\varepsilon = 0.5$ and permeability $\beta_i = 1.7 \times 10^{-10}$ m^2; $Re_{in} = 100$, $Re_m = 1.0$. When the inertial effects are considered, the coefficient B of the

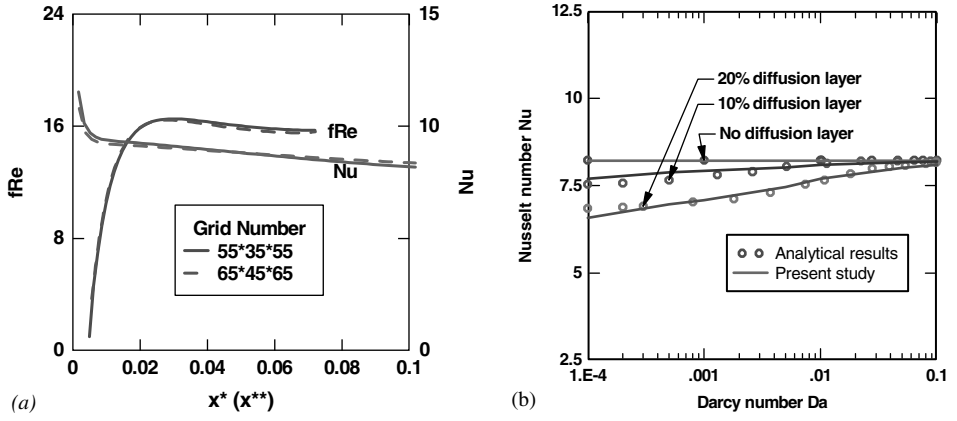

Fig. 2. (a) Influence of grid size on *fRe* and *Nu* and (b) fully developed *Nu* variation in a parallel plate duct with Darcy number ($Da = \beta/h$), compared with the analytical ones from [7].

porous anode layer, clarified in [7], is assumed according to $B = \varepsilon F/(\beta_i)^{0.5}$. Here, β_i is the permeability of the porous anode layer and the Forchheimer coefficient F is calculated by $F = 1.8/(1.8\varepsilon^5)^{0.5}$ [7]. Based on the base case data above, the three characteristics ratios are: $D_{hr} = 2$, $PL_r = 2$ and $PR_r = 0.012$, respectively. It should be noted that all the results presented hereafter are for the base case condition unless otherwise stated. However, parameter studies are conducted also for various ratios by changing h_d, b, h_p, β and U_{in}, respectively.

In order to evaluate the performance of the numerical method and code, test calculations considering grid sensitivity, code performance and validation were carried out. It is clear that the calculated *fRe* and *Nu* do not change significantly when the number of grid points is increased beyond $55 \times 35 \times 55$ (55×35 for the cross-section, 55 for the main flow direction) (see Fig. 2(a)). Calculations have been carried out for fully developed conditions in a parallel plate duct for various thickness of the porous layer. The comparison in Fig. 2(b) showed that the computed $\overline{Nu_b}$ values (*Nu* hereafter) agree well

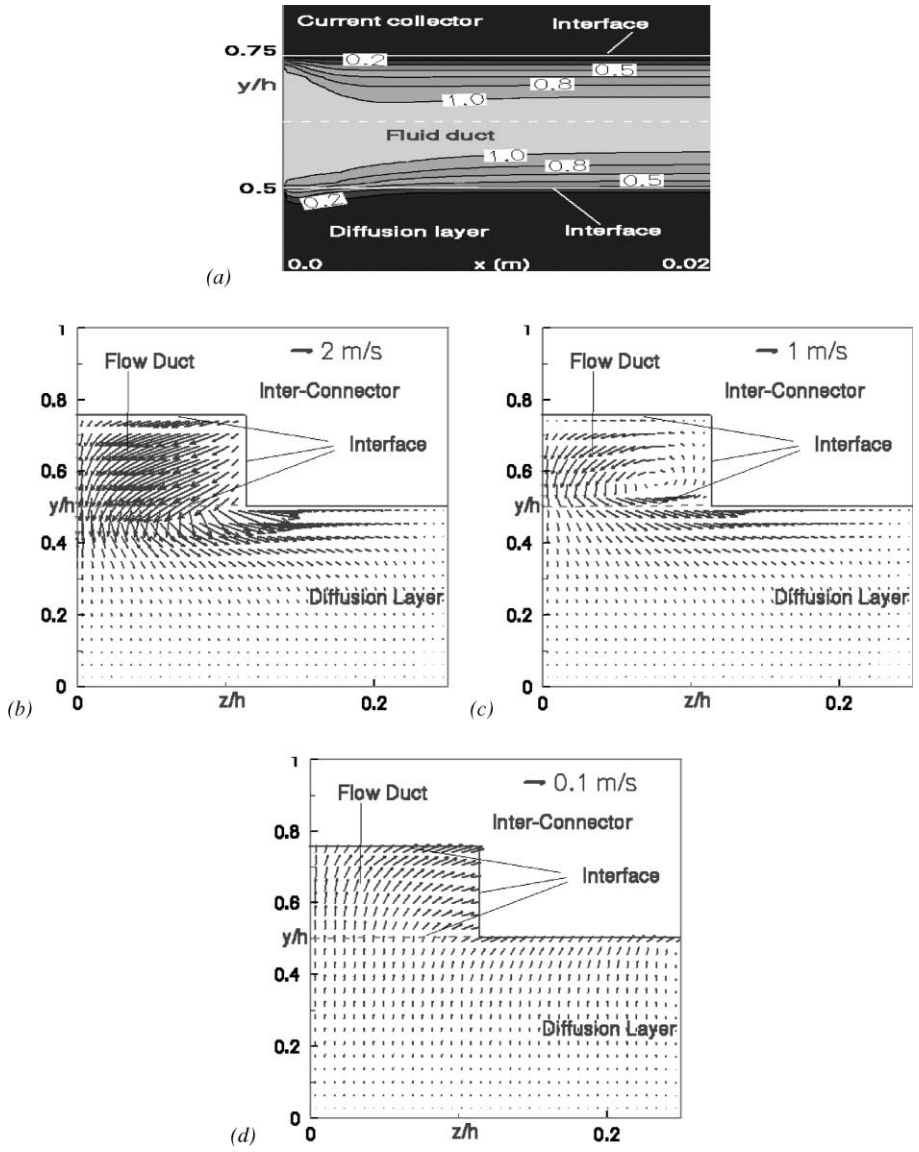

Fig. 3. (a) Dimensionless axial velocity contours (U/U_{in}) along main flow direction, (b,c,d) cross-section velocity vectors: (b) the inlet; (c) 1/6 length; and (d) the exit. Anode-supported SOFC duct for the base case condition.

with the analytical ones for the same boundary conditions, and the code is then considered sufficiently accurate for the main task of the present studies.

4. Results and discussion

In this section, the main results of the numerical simulations are reported and discussed. The gas flow and heat transfer of the duct are presented in terms of velocity profiles, friction factors, temperature profiles, Nusselt numbers for various parameters. These parameters include the diameter ratio D_{hr}, the permeation length ratio PL_r, the permeation rate ratio PR_r. Effects of the inertial force are assessed by the Forchheimer-extended Darcy model.

4.1. Analysis of various transport processes for the base case condition

To understand and clarify the gas flow and heat transfer mechanism, axial velocity contours (U/U_{in}) and cross-section velocity vectors are presented and discussed for an anode-supported duct for the base case condition. For a pure flow duct (without porous medium), it is clear that the axial velocity contours represent the development of the hydrodynamic boundary layer. There is a fluid acceleration in the core, which compensates the development of the boundary layer near the solid walls. It is also true that the axial velocity is uniformly developed, and a symmetry plane is located at the horizontal central plane (not shown in this study). As mentioned above, gas flow in the composite anode-supported SOFC duct is affected by the forced convection in the flow duct. The mass injection caused by the electrochemical reaction at the bottom wall and the gas permeation across the interface are also important. Due to the permeation and mass injection effects, the uniform distribution and the symmetry of the axial velocity does no longer exist, and the position of the maximum contour values shifts away from the central plane ($y/h = 0.625$ in Fig. 3(a)). The mass permeation, as clarified above, depends on the pressure gradients between the flow duct and the porous anode layer. It has the biggest value at the inlet because the pressure in the flow duct has its maximum while the minimum pressure appears in the porous anode layer. Thus more mass is permeated into the porous anode layer in the entrance area. As the consequence, part of the boundary is shifted into the porous anode layer, which can be verified by a change of the boundary layer thickness close to the interface in Fig. 3(a). This is the reason why the hydrodynamic boundary layer in the flow duct close to the interface becomes thinner in the entrance region (see Fig. 3(a)).

Fig. 3(b)–(d) show cross-section velocity vectors for selected longitudinal stations x^* (hydrodynamic dimensionless axial distance, $x/(D_h Re)$). The scale of the vector plot (i.e., 2.0 m/s in Fig. 3(b)) is a reference value of the maximum cross-section velocity. It should be noted that the reference vector is not the same in the figures. Fig. 3(b) is for the entrance region, while Fig. 3(c) is for the position 1/6 length from the inlet and Fig. 3(d) for the exit of the duct. It is clear from Fig. 3(b) that the cross-section velocity vectors are dominated by a strong downward flow into the porous anode layer from the flow duct. Small downward velocity vectors can be found in most of the porous layer except at the bottom regions. However, the permeation is stronger around the lower corner close to the vertical solid wall in the flow duct. The possible reason could be that gas from this corner is expanded and distributed into a wider area, i.e., not only to the area below it but also to the area of right part of the porous anode layer. To keep the mass and momentum balances, a flow from the mid-plane to the low corner of the duct can be found in Fig. 3(c) along the interface. However, this flow is turned up due to the fact that the side wall is solid (impermeable). Consequently, a weak secondary flow can be observed in the flow duct (see Fig. 3(c)).

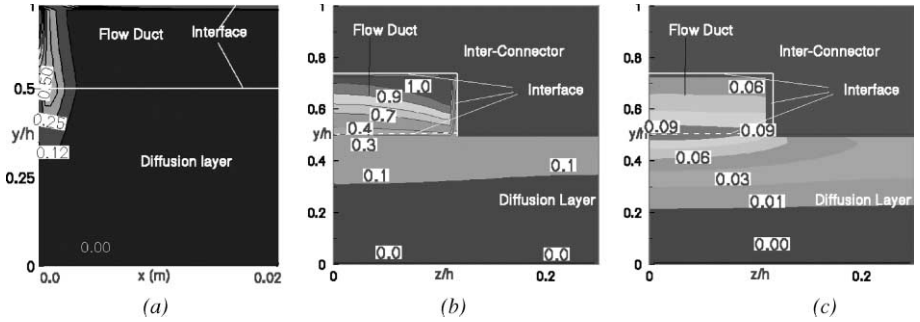

Fig. 4. Dimensionless pressure difference $(P - P_b)/(P - P_b)_{in}$ for: (a) main flow direction; cross-sections at; (b) the inlet; (c) 1/6 of the duct from the inlet. Base case condition.

Because the pressure in the flow duct will fall due to the friction as mentioned above, a decreased pressure gradient along the flow direction is expected. Consequently, gas permeation decreases and becomes weaker. The secondary flow caused by the permeation does no longer exist. Due to the blockage of the porous layer at the exit, moreover, the permeated gas turns up and returns into the flow duct, which can be found in Fig. 3(d) by the upward cross-section flow. From Fig. 3(a), it is confirmed that the hydrodynamic boundary layer moves back into the flow duct from the porous anode layer due to this back permeation. As shown in Fig. 3(b)–(d), the cross-section velocity is very small in the porous layer, i.e., of order 0.01 m/s in most of the region (except the region close to the interface) in Fig. 3(c), while in the flow duct the value is in the order 1 m/s. This indicates that the cross-section velocity in the porous layer is only some percent of that in the gas flow duct.

Normalized pressure gradients between the flow duct and the bottom surface of the porous anode layer $(P-P_b)/(P-P_b)_{in}$ are shown in Fig. 4, in which $(P-P_b)$ is the vertical pressure gradient (P_b the pressure at the bottom surface) in any cross-section along the main flow direction, while $(P-P_b)_{in}$ is the value at the inlet. From Fig. 4(a), which is only for the flow duct and the porous anode layer along the main flow direction, it is found that the pressure gradient appears mainly in the entrance region. Fig. 4(b) and (c) show the pressure gradient for the selected cross-sections, one is for the inlet, and another is for the 1/6 length from the inlet. It is revealed that the pressure gradient is significant in Fig. 4(b), but less significant in Fig. 4(c). This confirms that a big pressure gradient in the inlet gives a strong mass permeation across the interface (see Fig. 3(b)), while the weak permeation in Fig. 3(c) is due to the decreased pressure gradient (see Fig. 4(c)).

Fig. 5 shows the permeation Reynolds number Re_p, friction factor fRe and Nusselt number Nu along the main flow direction. Similar to the wall Reynolds number Re_m for mass transfer across the bottom wall, permeation Reynolds number is defined as $Re_p = V_p D_h/v$ for gas permeation across the interface. Here, V_p is the velocity caused by the gas permeation across the interface. It is found that Re_p has a large negative value (i.e., permeation into the porous anode layer) at the inlet region) (see Fig. 5(a)). Due to the decreasing pressure gradient along the duct, permeation into the porous layer becomes smaller. On the other hand, H_2O generation caused by the electrochemical reaction at the bottom wall, together with back permeation clarified above, contributes to a mass injection into the flow duct. This is confirmed by a small but positive (i.e., flowing back into the flow duct) Re_p shortly downstream the inlet in Fig. 5(a).

For a pure flow duct with impermeable walls, fRe decays rapidly from the inlet, and a constant value is approached when the convective gas flow is fully developed (see Fig. 5(b)). For the anode duct with a porous layer, a small friction factor fRe is observed at the inlet region but it increases along the main flow direction. The reason is that a big (negative) Re_p at the inlet region allows more gas to be transported from the flow duct. Similar to a suction flow from a duct, there is certainly a decrease in the friction factor from that of the pure forced convection (see [10]). For increasing x^*, the Re_p becomes smaller and its contribution to the decrease of fRe is less significant. This contribution will be zero when $Re_p = 0$. Along the flow direction beyond this position, the gas flow is possibly affected by the following mechanisms: secondary flow and back permeation to increase fRe, convective flow to decrease fRe. It can be clearly observed that fRe in Fig. 5(b) has almost constant characteristics after a certain distance of the duct, i.e., secondary flow and back permeation balance the effects of convective gas flow. The Nu for the composite duct has a similar behaviour as that of the pure

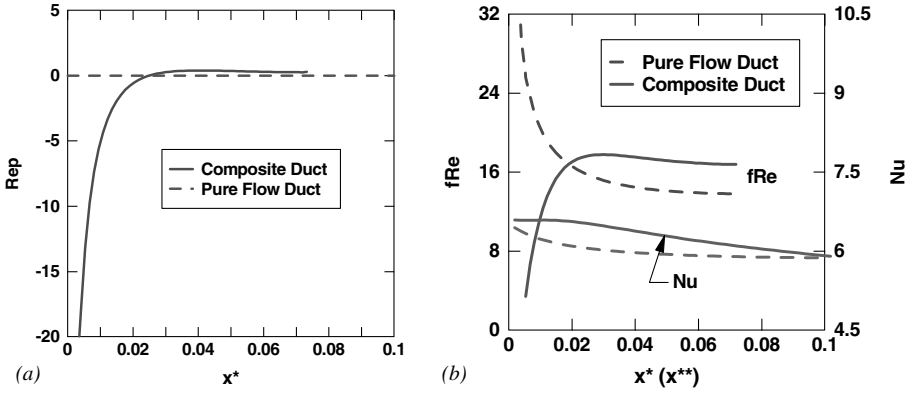

Fig. 5. (a) Permeation Reynolds number Re_p, (b) fRe and Nu along the main flow direction. Base case condition.

flow duct. However, a slightly bigger Nu is predicted for the composite duct, due to the mass permeation into the porous layer. From the discussion above, it is found that mass permeation across the interface has more significant effects on the gas flow than on heat transfer, both in the entrance region and further downstream. Parameter studies have been conducted also for gas flow and heat transfer in the composite duct, to find out the effects of duct configuration and operation parameters.

4.2. Effects of the diameter ratio

To investigate effects of the diameter ratio on the gas flow and heat transfer, the height of flow duct h_d was varied while other parameters were kept constant. Fig. 6 shows cross-section velocity vectors at selected positions for cases $D_{hr} = 1.67$ ($h_d = 1.6$ mm) and $D_{hr} = 2.33$ ($h_d = 0.75$ mm) (the base case $D_{hr} = 2$, $h_d = 1.0$ mm). The secondary flow, as clarified previously, appears in the flow duct at 1/6 length from the inlet for both D_{hr} conditions. It prolongs to the position at 1/3 length only for the case of a big D_{hr} (see Fig. 6(b)), while upward flow caused by the back permeation and mass injection is observed for the small D_{hr} (see Fig. 6(a)).

Fig. 7 shows a comparison of Re_p and fRe with those for the base case condition. From Fig. 7(a), it is clear that the distance from the inlet to the position where the sign of Re_p changes is shorter for small D_{hr} and longer for big D_{hr}. It can be found also that the permeation Reynolds number Re_p has a similar trend as that of the base case, except that it has a slightly bigger value for small D_{hr} and smaller value for big D_{hr}, after a certain distance downstreams the inlet. However, back permeation only happens for the case of the small D_{hr}. In Fig. 7(b), there is a clear peak of fRe for the case $D_{hr} = 1.67$, but this does not occur for the case $D_{hr} = 2.33$. By comparing Fig. 7(a) and (b) for the small D_{hr}, it can be understood that the effect of the secondary flow and the back permeation, which increases fRe, is weak for the small D_{hr}. Pure forced convection flow then dominates the change in fRe for this case. Therefore, fRe is reduced from its peak value. For the case of the big D_{hr}, secondary flow dominates the cross-section flow, and fRe increases along the flow direction. It should be noted that effects of the diameter ratio D_{hr} on the heat transfer in terms of Nu are not so significant as those on the gas flow (not shown here).

4.3. Effects of permeation length ratio

Effects of the permeation length ratio have been investigated as well by varying the width of the flow duct

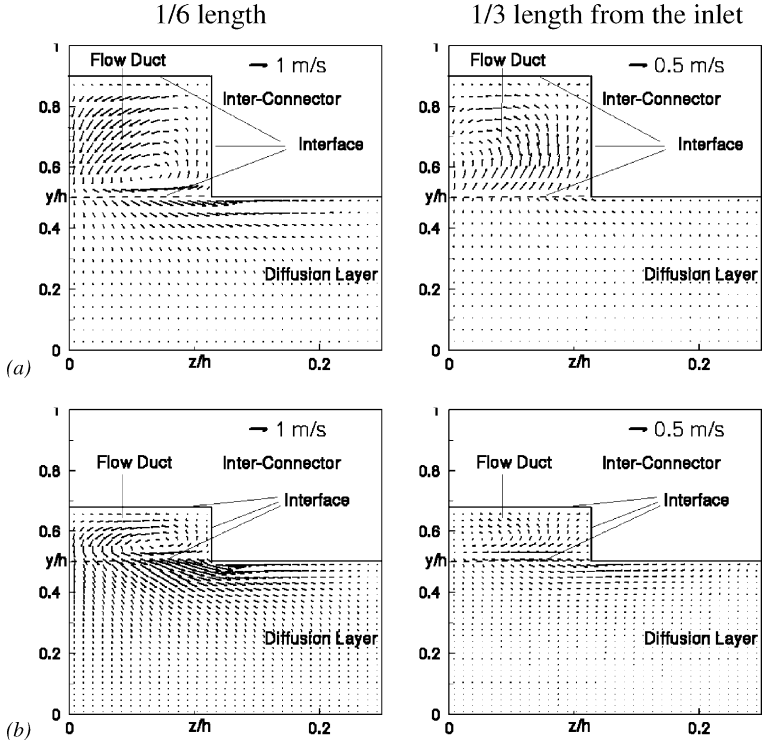

Fig. 6. Cross-section velocity vectors at selected positions for cases: (a) $D_{hr} = 1.67$, (b) $D_{hr} = 2$.

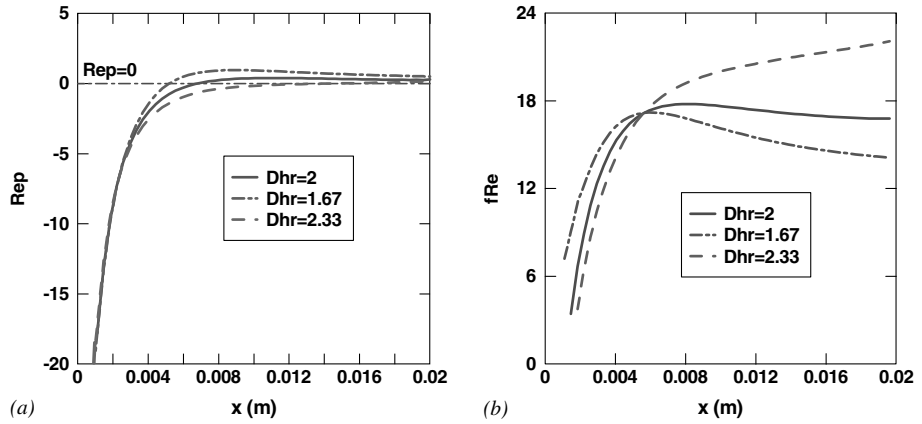

Fig. 7. Effects of the diameter ratio D_{hr} on: (a) permeation Reynolds number Re_p, (b) fRe.

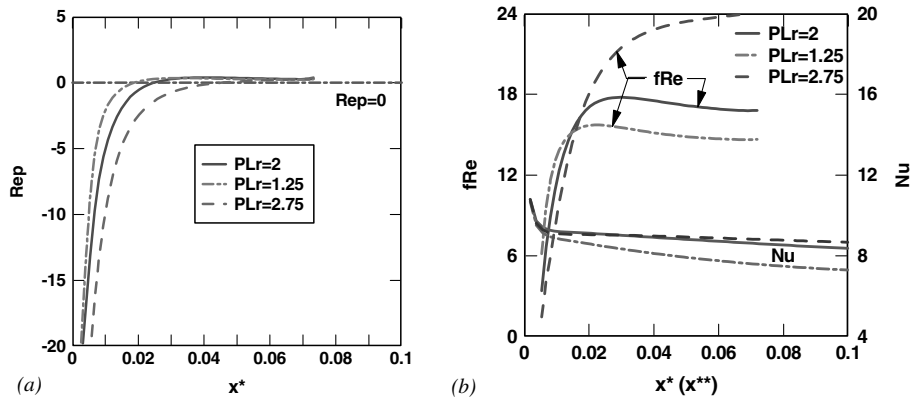

Fig. 8. Effects of the permeation length ratio PL_r on: (a) permeation Reynolds number Re_p and (b) fRe and Nu.

b, while other ratios were kept constant. Permeation length ratios $PL_r = 1.25$ ($b = 1.6$ mm) and $PL_r = 2.75$ ($b = 0.75$ mm) were employed and compared with the base case ($PL_r = 2$, $b = 1.0$ mm). In Fig. 8(a), the distance where Re_p changes sign is shorter for the small PL_r and longer for the big PL_r. It can be found that the permeation Reynolds number Re_p has small negative values for the small PL_r, and big negative values for the big PL_r. In Fig. 8(b), there is a peak value of fRe for the case of the small PL_r, but this is not true for another case ($D_{hr} = 2.33$). As clarified in the last section, the secondary flow and back permeation is weak and convective flow dominates the change in fRe for the case of the small PL_r. For the case of the big PL_r, secondary flow has more effects and fRe increases along the flow direction. As expected, similar conclusions from the effects of diameter ratio can be drawn here for permeation length ratio, i.e., big PL_r has more significant effects on the decrease in fRe at the entrance region, and the increase downstream. Calculated Nu numbers are shown in Fig. 8(b) also. It is found that big PL_r has effects on the increase in Nu, while small PL_r decreases Nu compared to the base case.

4.4. Effects of the permeation rate ratio

4.4.1. Permeability effects

Fig. 9 shows the impact of the porous layer permeability on the gas flow and heat transfer. It is noted from Fig. 9(a) that, by decreasing the permeability, Re_p has a small negative value at the entrance region. Permeability is a term used for the conductivity of the porous medium with respect to permeation by a fluid. It is known that a small permeability of a porous layer allows less gas to pass at the same pressure gradient. As a consequence, less significant impact on the decrease in fRe in the entrance region and increase afterwards are expected. From Fig. 9(b) it is found that for a small PL_r (permeability), fRe has the characteristics of that for the pure flow duct. However, Nu is decreased compared to the base case ($\beta_i = 1.7 \times 10^{-10}$), i.e., a small PR_r results in low Nu. It is worthwhile to note that a calculation was

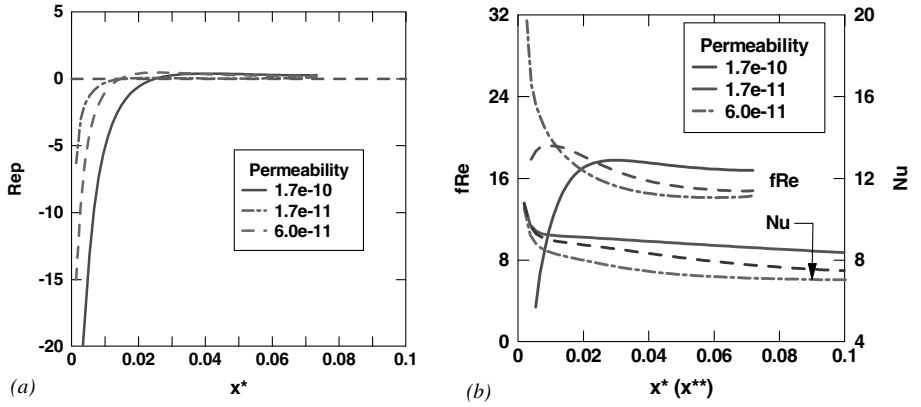

Fig. 9. Effects of the permeation rate ratio (permeability) on: (a) Re_p and (b) fRe and Nu.

conducted for a permeability ($\beta_i = 6.0 \times 10^{-11}$) between those, and the results show a slight changed fRe. For this case, Nu has a value that is in between the others.

4.4.2. Effects of inlet velocity

Effects of inlet velocity on the gas flow and heat transfer are shown in Fig. 10. Permeation rate ratios $PR_r = 0.024$ ($Re_{in} = 200$) and $PR_r = 0.006$ ($Re_{in} = 50$) have been employed to compare with the base case, i.e., $PR_r = 0.012$ and $Re_{in} = 100$. It is revealed that, in the entrance region, small PR_r has a small negative Re_p and therefore has a less significant effect on the decrease in fRe. Big PR_r on the other hand has more significant effect on the decrease in fRe because it has a big negative Re_p value. It is noted, from Fig. 10(a), that there is no back permeation for all the cases. fRe is controlled by the combined effects of the secondary flow in the cross-section and convective flow along the flow direction downstream the entrance region. The same conclusion for the heat transfer as in the last section can be drawn, i.e., small PR_r results in low Nu number.

4.4.3. Effects of porous layer thickness

As expected, thickness of the porous anode layer is one of the most important parameters. The effects on the transport processes have also been investigated in this paper. From Fig. 11(a), it is noted that the big PR_r (0.1 and 0.028) from thinner porous layer (thickness 0.23 and 0.86 mm, respectively) predicts a small (not a big) negative Re_p, compared to those of the base case. Back permeation is not observed for big PR_r cases (thin permeation layers). This is due to the fact that the thickness of the porous layer has opposite roles in the diameter ratio and permeation rate ratio, i.e., a thinner porous layer generates a smaller diameter ratio D_{hr}, however a bigger permeation rate ratio. As a result, the thickness of the porous layer has composite effects on the transport processes.

As shown in Fig. 11(b), a thin porous layer (big PR_r) has less effect on both the decrease in fRe in the entrance region, and the increase in fRe downstream. It is also clear that the distance where fRe decreases becomes shorter for the bigger PR_r. This is because the distance

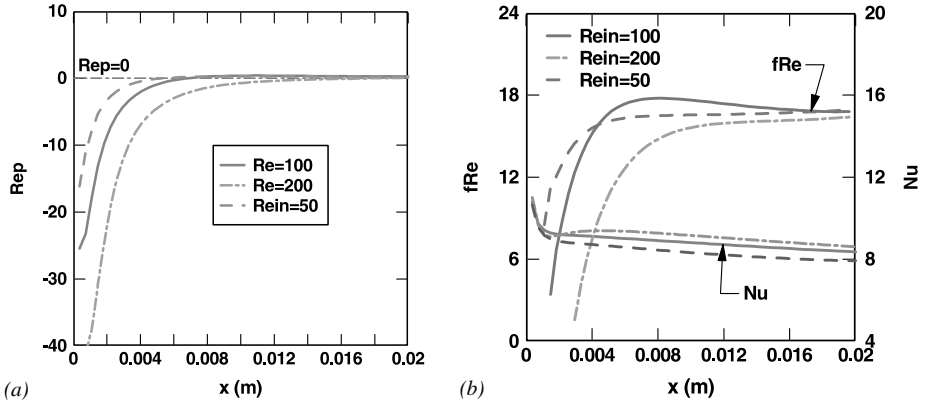

Fig. 10. Effects of the permeation rate ratio (inlet velocity) on: (a) Re_p and (b) fRe and Nu.

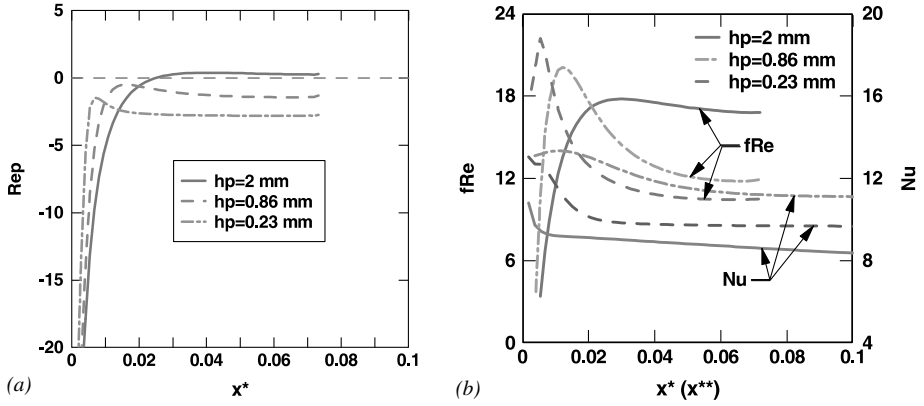

Fig. 11. Effects of the permeation rate ratio (thickness of the porous layer) on: (a) Re_p and (b) *fRe* and *Nu*.

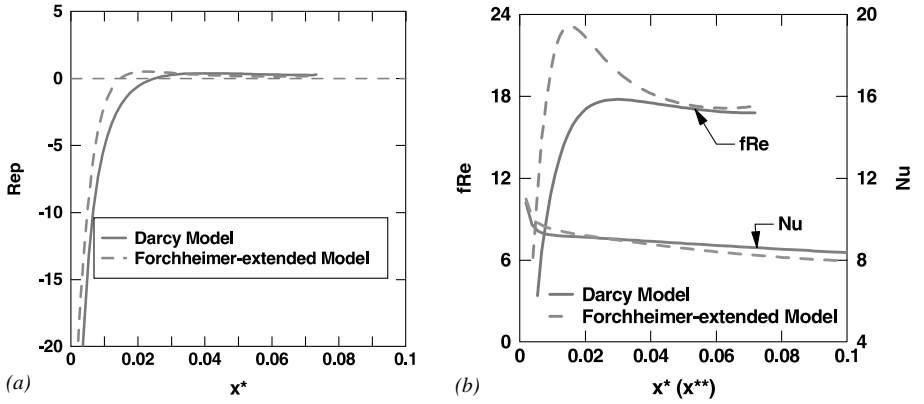

Fig. 12. Effects of the inertial force on: (a) Re_p and (b) *fRe* and *Nu*.

where big negative Re_p values occur is shorter for the big PR_r, i.e., strong mass permeation for thinner porous layer happens at a shorter downstream distance. By referring to Fig. 11(b), it is found that big *Nu* has been predicted for both cases of the thinner porous layer compared to the base case, this is so because the contribution of mass permeation happens in the whole duct (see Fig. 11(a)). However, the duct with a thicker porous layer ($h_p = 0.86$ mm) shows bigger *Nu* than those of a thinner layer ($h_p = 0.23$ mm). As clarified in [7], there is no clear trend in the effect of the porous layer thickness on the Nusselt number.

4.5. Effects of inertial force

Comparisons of Re_p, *fRe* & *Nu*, simulated by the Darcy model and the Forchheimer-extended model, are presented in Fig. 12. It is clear that the Forchheimer-extended model predicts a small negative Re_p and an earlier change of its sign from negative to positive (see Fig. 12(a)). As discussed earlier in the last section, a less significant effect on the change of *fRe* and *Nu* is expected. This is due to the fact that the inertial force in Eq. (5) has a similar contribution as the Darcy force, and resembles an extra retarding force for the gas flow in the porous anode layer. From Fig. 12(b), it can be observed that the decrease in *fRe* in the entrance region and the increase downstream are less significant if compared to those predicted by the Darcy model. For the heat transfer, both cases generate similar *Nu*, consequently the same conclusion can be drawn, i.e., less significant effects on the heat transfer.

5. Conclusions

Simulation and analysis have been conducted for gas flow and heat transfer in a duct of anode-supported SOFCs. Unique fuel cell conditions were applied in a fully three-dimensional calculation method for investigation of various transport processes, such as developing convective flow and heat transfer, gas permeation,

and mass transfer. The considered composite duct consists of a thick porous anode layer, gas flow duct, and solid current interconnector.

It has been revealed that the value of *fRe* and *Nu* varies widely. For the base case condition, *fRe* decrease from that of pure flow duct and has a low value due to the permeation effects in the entrance. The secondary flow developed in the flow duct and back permeation increase *fRe* from a certain position in the main flow direction. By varying one or more of the characteristic ratios identified in this paper, effects of permeation and secondary flow on the gas flow and heat transfer have been investigated in terms of *fRe* and *Nu*. A uniform *fRe* in the main flow direction can be achieved through appropriate adjustment of the flow parameters or/and duct configuration. This study may be used for the anode supported SOFC modeling, as a design tool/adjustment of the flow duct configuration to establish prescribed flow conditions and heat transfer, or establish the flow distribution and heat transfer for a given configuration. It should be noted that any radiation effects (maybe significant close to the bottom surface where the electrochemical reactions occur) have not been included in this study.

Acknowledgement

The current research is financially supported by the National Fuel Cell Programme by the Swedish Energy Administration.

References

[1] A.V. Virkar, J. Chen, C.W. Tanner, J.W. Kim, The role of electrode microstructure on activation and concentration polarizations in solid oxide fuel cells, Solid State Ionics 131 (2000) 189–198.

[2] H. Yakabe, M. Hishinuma, M. Uratani, Y. Matsuzaki, I. Yasuda, Evaluation and modeling of performance of anode-supported solid oxide fuel cell, J. Power Sourc. 86 (2000) 423–431.

[3] W. Lehnert, J. Meusinger, F. Thom, Modelling of gas transport phenomena in SOFC anodes, J. Power Sourc. 87 (2000) 57–63.

[4] T. Ackmann, L.G.J. Haart, W. Lehnert, F. Thom, Modelling of mass and heat transport in thick-substrate thin-electrolyte layer SOFCs, Proceedings of the 4th European Solid Oxide Fuel Cell Forum, Lucerne/Switzerland, July 2000, pp. 431–438.

[5] J. Yuan, M. Rokni, B. Sundén, Analysis of fluid flow and heat transfer in proton exchange membrane fuel cell ducts by an extended darcy model, in: S. Dost, H. Struchtrup, I. Dincer (Eds.), Progress in Transport Phenomena, 2002, pp. 837–842.

[6] H. Teng, T.S. Zhao, An extension of darcy's law to non-stokes flow in porous media, Chem. Eng. Sci. 55 (2000) 2727–2735.

[7] M.K. Alkam, M.A. Al-Nimr, M.O. Hamdan, Enhancing heat transfer in parallel-plate channels by using porous inserts, Int. J. Heat Mass Transfer 44 (2001) 931–938.

[8] B. Alazmi, K. Vafai, Analysis of fluid flow and heat transfer interfacial conditions between a porous medium and a fluid layer, Int. J. Heat Mass Transfer 44 (2001) 1735–1749.

[9] J. Wang, Z. Gao, G. Gan, D. Wu, Analytical solution of flow coefficients for a uniformly distributed porous channel, Chem. Eng. J. 84 (2001) 1–6.

[10] J. Yuan, M. Rokni, B. Sundén, Simulation of fully developed laminar heat and mass transfer in fuel cell ducts with different cross sections, Int. J. Heat Mass Transfer 44 (2001) 4047–4058.

[11] J. Yuan, M. Rokni, B. Sundén, Buoyancy effects on developing laminar gas flow and heat transfer in a rectangular fuel cell duct, Numer. Heat Transfer 39 (2001) 801–822.

[12] J. Yuan, M. Rokni, B. Sundén, A numerical investigation of gas flow and heat transfer in proton exchange membrane fuel cells, Numer. Heat Transf., submitted for publication.

[13] L. Davidson, B. Farhanieh, *CALC_BFC*, Publication Nr 92/4, Chalmers University of Technology, Sweden 1991.

[14] M. Rokni, Numerical investigation of turbulent fluid flow and heat transfer in complex ducts, Doctoral Thesis, ISSN 1104-7747, Division of Heat Transfer, Lund Institute of Technology, Sweden, 1998.